Verifying the Blade Element Momentum Method in unsteady, radially varied, axisymmetric loading using a vortex ring model.

Yu, Wei; Simao Ferreira, Carlos; van Kuik, Gijs; Baldacchino, Daniel

DOI
10.1002/we.2005

Publication date
2016

Document Version
Final published version

Published in
Wind Energy

Wind Energy

WIND ENERGY
Wind Energ. (2016)
Published online in Wiley Online Library (wileyonlinelibrary.com). DOI: 10.1002/we.2005

RESEARCH ARTICLE

Verifying the Blade Element Momentum Method in unsteady, radially varied, axisymmetric loading using a vortex ring model

Wei Yu, Carlos Simao Ferreira, Gijs van Kuik and Daniel Baldacchino

Faculty of Aerospace Engineering, Delft University of Technology, Kluyverweg 1, 2629 HS, Delft, The Netherlands

ABSTRACT

Although the Blade Element Momentum method has been derived for the steady conditions, it is used for unsteady conditions by using corrections of engineering dynamic inflow models. Its applicability in these cases is not yet fully verified. In this paper, the validity of the assumptions of quasi-steady state and annuli independence of the blade element momentum theory for unsteady, radially varied, axi-symmetric load cases is investigated. Firstly, a free wake model that combines a vortex ring model with a semi-infinite cylindrical vortex tube was developed and applied to an actuator disc in three load cases: (i) steady uniform and radially varied, (ii) two types of unsteady uniform load and (iii) unsteady radially varied load. Results from the three cases were compared with Momentum Theory and also with two widely used engineering dynamic inflow models—the Pitt-Peters and the Øye for the unsteady load cases. For unsteady load, the free wake vortex ring model predicts different hysteresis loops of the velocity at the disc or local annuli, and different aerodynamic work from the engineering dynamic inflow models. Given that the free wake vortex ring model is more physically representative, the results indicate that the engineering dynamic inflow models should be improved for unsteady loaded rotor, especially for radially varied unsteady loads. © 2016 The Authors. *Wind Energy* Published by John Wiley & Sons, Ltd.

KEYWORDS

free wake vortex ring; actuator disc; radially varied load; unsteady load; dynamic inflow; quasi-steady; annuli independent assumption

Correspondence

Wei Yu, Faculty of Aerospace Engineering, Delft University of Technology, Kluyverweg 1, 2629 HS, Delft, The Netherlands.
E-mail: W.Yu@tudelft.nl

Received 17 April 2015; Revised 24 May 2016; Accepted 26 May 2016

NOMENCLATURE

$\bar{v}_z$	averaged axial velocity $[ms^{-1}]$
Γ	strength of vortex ring $[m^2s^{-1}]$
γ	strength of semi-infinite vortex tube $[ms^{-1}]$
Ω	solid angle $[steradian]$
ρ	fluid density $[kgm^{-3}]$
τ	non-dimensionalized time $\left(\tau = \frac{t \cdot V_0}{R}\right)$ $[-]$
τ_1	time constant $[s]$
τ_2	time constant $[s]$
$\vec{f}$	the force density on the flow $[Nm^{-3}]$
A	rotor area $[m^2]$
C_t	thrust coefficient $[-]$

D	diameter of the actuator disc $[m]$
k	reduced frequency $\left(k = \frac{\omega D}{2V_0}\right)$ $[-]$
R	radius of the actuator disc $[m]$
r	radial coordinate $[m]$
R_i	radius of i^{th} vortex ring $[m]$
R_{tube}	radius of the semi-infinite vortex tube $[m]$
T	thrust $[N]$
V_0	free stream velocity $[ms^{-1}]$
v_r	radial velocity $[ms^{-1}]$
v_r^{ind}	radial induced velocity $[ms^{-1}]$
v_z	axial velocity $[ms^{-1}]$
v_z^{ind}	axial induced velocity $[ms^{-1}]$
v_{int}^{ind}	intermediate induced velocity $[ms^{-1}]$
v_{qs}^{ind}	quasi-steady induced velocity $[ms^{-1}]$
z	axial coordinate $[m]$
BEM	Blade Element Momentum Method
FWVR	Free Wake Vortex Ring
MT	Momentum Theory
MT + Øye	the Øye dynamic inflow model applied to Momentum Theory
MT + P − P	the Pitt-Peters dynamic inflow model applied to Momentum Theory

1. INTRODUCTION

The Blade Element Momentum Theory (BEM) is based on the actuator disc momentum theory and the blade element theory. Hansen *et al.*[1] pointed out that the accuracy of BEM is acceptable at normal load conditions if satisfactory airfoil data are provided.

There are two main intrinsic assumptions in the BEM model. One is the equilibrium state assumption of Momentum Theory. However, the load on wind turbines is unsteady, which is determined by the non-stationary environment. The limits of the effectiveness of velocity prediction by BEM in unsteady load cases are unknown yet. This is relevant for the flexible blade structures of large-scale turbines, and the different kinds of passive and active aerodynamic control strategies, such as yaw, pitch control and smart rotor control, where wind turbines operate in a highly unsteady state. Current approach to overcome this limitation of BEM is to use engineering dynamic inflow models. Various dynamic inflow models were proposed based on engineering or physical models and summarized by Snel and Schepers.[2] These models were tested against measurements by Snel and Schepers.[3,4] Sørensen and Myken[5] obtained a non-linear and unsteady actuator disc model using a time-dependent vorticity-streamfunction formulation, but Chattot[6] pointed out that errors will be introduced with this method because vorticity diffuses from the slip line unphysically. Chattot[6] tried to extend the steady actuator disc theory to unsteady flow using a linear vortex ring modelling.

Another inherent limitation of BEM is the assumption of radial independence of flow passing through each adjacent annulus. According to Sørensen and Kock,[7] this assumption is acceptable, except for regions where load changes abruptly, for example, at the root and the tip region. Another situation where this assumption might not be applicable is distributed aerodynamic control, where there are local load variations due to distributed aerodynamic devices (e.g. trailing edge flaps or micro-tabs). Sørensen *et al.*[8] estimated up to 3% difference in the induced velocity between BEM and the CFD model, this model was developed by Sørensen[7] for uniform load. Madsen[9] proved that the momentum strip theory of BEM is unacceptable, especially at the tip and the root regions, using a near wake model.[10] The annuli were shown to be not independent; the pressure at the boundary of the annuli were suggested by van Kuik and Lignarolo[11] to be included in the momentum theory to remedy the effect of annuli independent assumption. Conway[12] obtained a linear solution for an actuator disc with steady heavy loads, which was extended to a semi-analytical non-linear method to consider certain distributions of radially varied loads.[13]

However, many dynamic inflow models are based on the same independent annuli assumption of BEM. To date, only specific radially varied load and unsteady load of an actuator disc have been discussed separately in previous studies.[10,13] In this work, the validity of BEM with engineering dynamic inflow models in predicting the induction of an actuator disc with unsteady, radially varied load is investigated using a free wake vortex ring (FWVR) model. The time-dependent modelling can handle unsteady loads intrinsically. The vortex rings are expanding or contracting freely because of the radial velocity

induced by all the vortex rings and the semi-infinite cylindrical vortex tubes. Local pressure gradient caused by locally varied load can be considered in this model.

In Section 2, the approaches and used models are detailed, the development of the FWVR model is firstly described, and then the two engineering dynamic inflow models are briefly introduced. Results are presented in Section 3 for three load cases: (i) steady uniform and radially varied load, (ii) two types of unsteady uniform load and (iii) unsteady radially varied load. Additionally, the effect of dynamic induction on aerodynamic work is also discussed. Conclusions are drawn in Section 4. A convergence study and the validity of the FWVR model are addressed separately in Appendix A and Appendix B.

2. APPROACHES AND MODEL DEVELOPMENT

2.1. Load cases

A variety of load cases are performed in the FWVR model to evaluate the dynamic induction of an actuator disc with different types of load. Velocity calculated from the FWVR model is compared with that of Momentum Theory and also with engineering dynamic inflow models of Pitt-Peters and Øye for the unsteady load cases. The three load case categories are listed in Table I.

$C_t = 7/9$ is treated as a baseline load case; the temporally and radially varied load are based on it. For Case I (a) and (b), a local radially varied load is prescribed at the annulus of $0.6R-0.8R$, a uniform steady load Case I (0) is given as reference. In Case II (1), a step uniform time-varying load is considered, while Case II (2) prescribes a harmonically time-varying

Table I. Load cases.

Load cases	uniform	radially varied
steady	I. 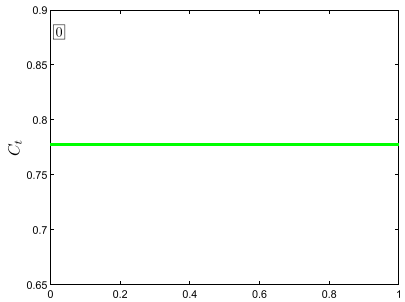	I. 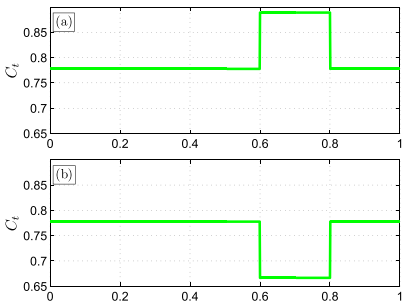
unsteady step	II.(1). 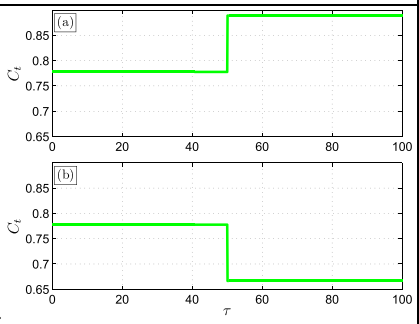	
unsteady harmonic	II.(2). 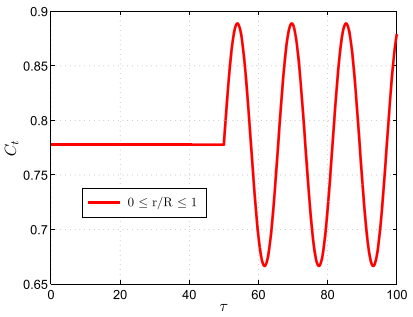	III. 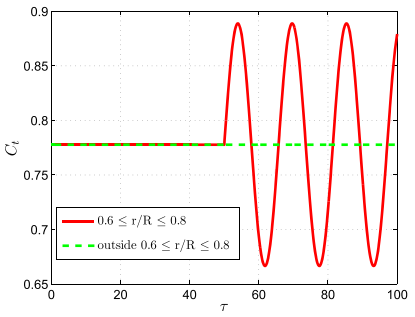

uniform load. Lastly, a combination of the parameters in Case I and II is prescribed as III, where a harmonically time-varying radially varied load is applied at $0.6R - 0.8R$.

In Cases II and III, the unsteady load occurs at $\tau = 50$ when the velocity is converged for $C_t = 7/9$. The amplitude of harmonic load is $\Delta C_t = 1/9$. The harmonic reduced frequencies in Cases II (2) and III are 0.05, 0.2, 0.5, 1, when non-normalizing using $k = \frac{\omega D}{2V_0}$. The time and velocity presented in the results are non-dimensionalized using $\tau = \frac{V_0 t}{R}$ and the incoming wind speed V_0, respectively.

2.2. Model development

The development of the FWVR model will be firstly presented in this section. It is followed by the introduction of the two engineering dynamic inflow models of Pitt-Peters and Øye. The two dynamic inflow models will be applied to Momentum Theory on the entire actuator disc for Case II and applied to each annulus for Case III, for comparison with the FWVR model.

For an incompressible, inviscid fluid, the motion of the fluid particles, is governed by the Euler equation

$$\rho \frac{D\vec{v}}{Dt} = -\nabla p + \vec{f} \tag{1}$$

and the continuity equation

$$\nabla \cdot \vec{v} = 0 \tag{2}$$

where $\vec{v}$ is the velocity factor, $\vec{f}$ is the force density distribution that the body acts on the flow, ρ is the fluid density and p is the static pressure. The concept of the actuator disc was introduced by Froude,[14] where the rotor plane is treated as an actuator disc with an infinite number of blades. When wake rotation can be neglected, the vortex tube of actuator disc can be treated as distributed ring vortices along the tube surface shed from the edge of actuator disc and extended to the infinite downstream.[12]

The vortex surface is modelled as discrete vortex rings, which are shed from any radial location of the disc's surface where the local pressure gradient is non-zero. In axial and axi-symmetric flow, $\vec{f} = \vec{e}_z f$. Integrating it across the thickness dz of the disc yields a pressure jump $\Delta p = \int f dz$. Van Kuik[15] obtained a relationship between vortex strength and pressure jump, given by

$$\frac{D\Gamma_{edge}}{Dt} = \frac{\Delta p}{\rho} \tag{3}$$

The wake model is segregated into the near wake and the far wake, similar to the work from Øye[16] and van Kuik[11] for a steady load case. In this paper, the near wake is modelled by dynamic surfaces, consisting of free vortex rings shed from the edge of the actuator disc or other radial locations of the disc's surface where the local pressure gradient is non-zero; the far wake is represented by semi-infinite cylindrical vortex tubes with constant strength and radius. The vortex rings are considered as thin, axi-symmetric and uniform. Axi-symmetric rings mean that rings may expand or contract, their central axis always coinciding with the axis of the actuator disc. Figure 1 illustrates the vortex model schematically. The wake consists of numerous vortex rings for the near wake and semi-infinite vortex tubes for the far wake. The vortex sheds radially where there is a pressure jump.

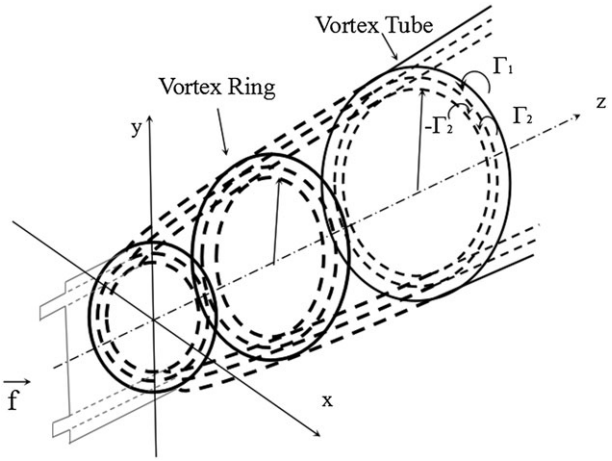

Figure 1. Scheme of the vortex model. The wake consists of vortex rings for the near wake and semi-infinite vortex tubes for the far wake.Vortex shed at the edge and positions where there is a pressure jump.

2.2.1. Near wake model.

As shown in equation 3, the strength of the unsteady vortex surface grows in time. The gain in circulation of the newly generated vortex ring as it passes through the edge of an annulus with non-zero pressure gradient is

$$\frac{\Gamma}{\Delta t} = \frac{\Delta p}{\rho} \tag{4}$$

From the definition of thrust coefficient, it follows that

$$C_t = \frac{T}{\rho A V_0^2/2} = \frac{A\Delta p}{\rho A V_0^2/2} \tag{5}$$

where T is thrust on the disc, A is the area of the disc and V_0 is the undisturbed wind speed. Combining equation 4 with 5, the relationship between the strength of the new vortex ring produced in time Δt and thrust coefficient is given by

$$\Gamma = C_t(V_0^2/2)\Delta t. \tag{6}$$

The analytical formulas for the velocity field induced by an infinitely thin axi-symmetric vortex ring are given by Yoon and Heister.[17] Figure 2 shows the cartesian coordinate system used in this paper for velocity field calculation. When the actuator disc is located at the $z = 0$ plane with the centreline along z-axis, the axial and radial velocities at an arbitrary point P in the field induced by the i^{th} vortex ring are given by

$$v_z^{ind} = \frac{\Gamma_i}{2\pi\sqrt{(z_p - z_i)^2 + (r_p + R_i)^2 + \delta}}\left[K(m^2) + \frac{R_i^2 - r_p^2 - (z_p - z_i)^2}{(z_p - z_i)^2 + (r_p - R_i)^2 + \delta}E(m^2)\right] \tag{7}$$

$$v_r^{ind} = -\frac{(z_p - z_i)\Gamma_i}{2\pi r_p\sqrt{(z_p - z_i)^2 + (r_p + R_i)^2 + \delta}}\left[K(m^2) - \frac{R_i^2 + r_p^2 + (z_p - z_i)^2}{(z_p - z_i)^2 + (r_p - R_i)^2 + \delta}E(m^2)\right] \tag{8}$$

where $< z_p, r_p >$ are the field coordinates of point P where the velocity is to be calculated, z_i is the axial coordinate and R_i is the radius of i^{th} vortex ring. $K(m)$ and $E(m)$ are the complete elliptic integrals of the first and second kind, where m is given by

$$m^2 = \frac{4r_pR_i}{(z_p - z_i)^2 + (r_p + R_i)^2 + \delta} \tag{9}$$

The method from Abramowitz *et al.*[18] is used for evaluating the first and second kind integrals. When the evaluation point P is too close to the vortex ring, there is an unphysically large induced velocity at that point. There are two commonly used methods to remove the singularity, one is to use a cut-off, the other is to apply a viscous vortex model with a finite core size.[19] The scheme of merging vortex elements when they are getting close to each other may offer a third option to avoid the singularity. A small cut-off δ is used in this paper, its effect is discussed in the Appendix A.

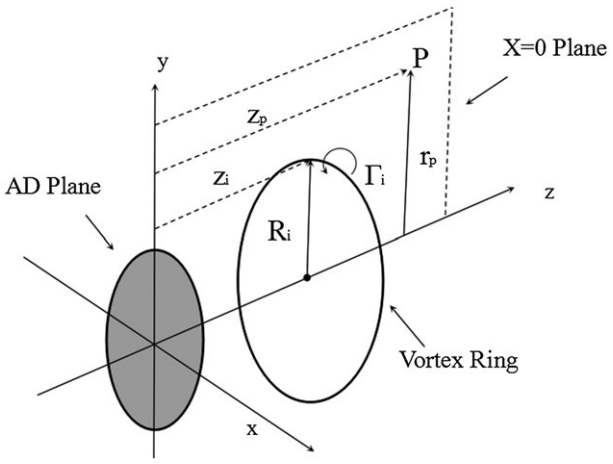

Figure 2. A schematic of coordinate system for computing induced velocity at arbitrary field points.

A vortex ring will induce a velocity in the entire flow field and on itself. The self-induced velocity is not negligible, but it cannot be calculated directly from equations 7 and 8 because of the singularity. There are different ways compared by Baldacchino[20] to solve this problem. Although the self-induced velocity represented by the induced velocity evaluated at the ring centroid is not theoretically correct, Baldacchino[20] showed the difference tends to zero when the ratio between the core radius and ring radius tends to zero. Infinitely thin vortex rings are assumed in this paper, and it is acceptable to use the induced velocity at the centre of each ring. The self-induced axial velocity v_z^s and radial velocity v_r^s are given by

$$v_z^s = \frac{\Gamma}{2R_i} \tag{10}$$

$$v_r^s = 0 \tag{11}$$

The radial and axial positions of the vortex rings are updated using a second order Euler method as follows

$$z_i^n = z_i^{n-1} + \left({v_{z(i)}}^{n-1} + V_0\right)\Delta t + \frac{1}{2}\frac{\left({v_{z(i)}}^{n-1} + V_0\right) - \left({v_{z(i)}}^{n-2} + V_0\right)}{\Delta t}(\Delta t)^2 \tag{12}$$

$$R_i^n = R_i^{n-1} + {v_{r(i)}}^{n-1}\Delta t + \frac{1}{2}\frac{{v_{r(i)}}^{n-1} - {v_{r(i)}}^{n-2}}{\Delta t}(\Delta t)^2 \tag{13}$$

where $< z_i^n, R_i^n >$ represents axial and radial position of ith vortex ring at time step n, and $z_i^0 = 0$,$R_i^0 = R$. $< v_{z(i)}^n, v_{r(i)}^n >$ are the axial and radial velocity of the ith vortex ring induced by all vortex rings and the semi-infinite vortex tubes in the field at time step n. The influence of time step is discussed in Appendix A.

Theoretically, the shed vortex rings need an infinite long time to transport infinitely far, which is impractical. To make it more practical while keep the model physically correct, the far wake is replaced by a semi-infinite cylindrical vortex tube. It happens after a sufficiently large time, when the shedding and transporting vortex ring system approach a steady state.

2.2.2. Far wake model.

The far wake part is represented by a semi-infinite cylindrical vortex tube, for which the vortex strength density should match that of the near wake part; it is given by

$$\gamma = \frac{\Gamma}{\Delta s} \tag{14}$$

where Δs should be the distance of adjacent rings in the ideal situations where the rings are uniformly spaced. Because of the vortex dynamics, the distance between adjacent rings are not the same (Figure A3). Alternatively, the averaged value of the distance of rings in the fully developed wake excluding the expansion part is used. Taking the case of $C_t = 8/9$ in Figure A3 as an example, the far wake is replaced at 11R, the near wake fully expands at 4R, $\Delta s = \frac{11R-4R}{N}$, N is the number of rings between 4R and 11R.

The axial velocity induced by the semi-infinite cylindrical vortex tube can be calculated from the analytical solution from van Kuik[11]

$$v_z^{ind} = \frac{\gamma}{4\pi}\Omega(z_0) \tag{15}$$

where Ω (defined in Paxton[21]) is the solid angle that the tube opening subtends to the position (z_p, r_p), where the velocity field is to be evaluated. The radial velocity is calculated using the following analytical equation from Branlard[22]

$$v_r^{ind} = -\frac{\gamma}{2\pi}\sqrt{\frac{R_{tube}}{r_p}}\left[\frac{2-m^2}{m}K(m^2) - \frac{2}{m}E(m^2)\right] \tag{16}$$

where $K(m^2)$ and $E(m^2)$ are the complete elliptic integrals of the first and second kind, and m is given in equation 9 by replacing (z_i, R_i) with (z_{tube}, R_{tube}).

The FWVR model is validated against wind tunnel measurements of a steady actuator disc model, which is presented in the Appendix B.

2.3. Empirical dynamic inflow models for BEM

Several empirical dynamic inflow models were developed previously to correct BEM by Snel and Schepers.[2,4] Two of the most commonly used models are the Pitt-Peters dynamic inflow model[23] and the Øye dynamic inflow model.[4]

2.3.1. The Pitt-Peters dynamic inflow model.

The Pitt-Peters dynamic inflow model was developed for an actuator disc with an assumed inflow distribution across the disc. It has received substantial validation in the field of helicopter aerodynamics.[4] Based on the assumption that the equation of Pitt-Peters can be applied to a blade element or actuator annulus level, the model was used in wind turbine unsteady load analysis by Snel and Schepers[4] and in several aerodynamic codes. When applied to a blade element or an actuator annulus, the dynamic inflow equation for each annular ring becomes

$$\frac{1}{\rho A_j V_0^2/2}\left[\frac{8}{3\pi}\rho A_j r_j \frac{dv_j^{ind}}{dt} + 2\rho A_j v_j^{ind}\left(V_0 + v_j^{ind}\right)\right] = C_{tj} \tag{17}$$

where j indicates the *j*th annular ring, A_j is the area of the *j*th annulus and v_j^{ind} is its azimuthal averaged induced velocity. The first term inside the outer bracket of equation 17 represents the additional force on the rotor disc resulting from the accelerating inflow,[24] while the second term results from the static pressure difference across the actuator disc.

2.3.2. The Øye dynamic inflow model.

In the Øye dynamic inflow model, the induced velocity is estimated by filtering the quasi-steady values through two first-order differential equations

$$v_{int}^{ind} + \tau_1 \frac{dv_{int}^{ind}}{dt} = v_{qs}^{ind} + b \cdot \tau_1 \frac{dv_{qs}^{ind}}{dt} \tag{18}$$

$$v_z^{ind} + \tau_2 \frac{dv_z^{ind}}{dt} = v_{int}^{ind} \tag{19}$$

where v_{qs}^{ind} is the quasi-steady value from BEM, v_{int}^{ind} is an intermediate value and the final filtered value v_z^{ind} is treated as the induced velocity. After calibration using a vortex ring model,[16] the two time constants are recommended as follows[2]

$$\tau_1 = \frac{1.1}{(1 - 1.3a)}\frac{R}{V_0} \tag{20}$$

$$\tau_2 = \left(0.39 - 0.26\left(\frac{r_j}{R}\right)^2\right)\tau_1 \tag{21}$$

where a is the axial induction factor, R is the rotor radius, r_j is the radius of *j*th annulus, and b is a constant value of 0.6.

3. RESULTS AND ANALYSIS

This section focuses on the analysis of the velocity field obtained from the FWVR model for the load cases in Table I, the results will be compared with Momentum Theory for all three cases and also compared with the two engineering dynamic inflow models of the Pitt-Peters and Øye for Cases II and III.

3.1. Analysis for Case I—steady uniform and radially varied load

The results for Case I are discussed in this section. All data for Figures 3–5 are obtained at $\tau = 50$.

Figure 3 compares the distribution of axial velocity v_z at the actuator disc plane calculated from the FWVR model and Momentum Theory for the uniform load (Case I (0)), radially increased load (Case I (a)) and radially decreased load (Case I (b)). For Case I (0), v_z calculated from the FWVR model matches with that from Momentum Theory, but it is not as uniform as Momentum Theory predicts, especially at the edge of actuator disc, which was also found by Sørensen and van Kuik.[7,8,11] For Case I (a) and (b), the locally changed v_z captured by the FWVR model matches generally well with that from Momentum Theory.

Figure 4 shows the axial velocity v_z and radial velocity v_r obtained from the FWVR model at the actuator disc plane for Case I (0),(a),(b). We can see v_z and v_r change dramatically at the region $0.6R - 0.8R$ where load locally varied. Outside the local annulus, v_z and v_r change slightly compared with Case I (0). The slight change in velocity at other annuli shows that although the assumption of independent annuli is incorrect, its effect here is not significant. Another phenomenon is that v_z and v_r decrease sharply at the actuator disc edge, both of which keep decaying as the locations move outside from the centre of the disc.

Figure 5 shows v_z along the centreline from the FWVR model for the three types of load. It shows that the local load variation at the actuator disc has an effect on the entire flow field both downstream and upstream, albeit rather small. In Case I (b), v_z reaches steady state slightly faster than that of Case I (0), and the latter is slightly faster than that of Case I (a),

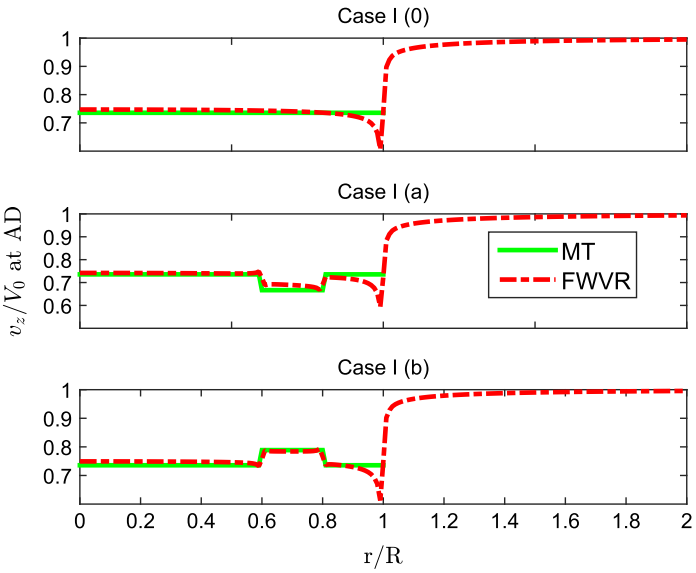

Figure 3. Comparison of the distribution of the axial velocity at the actuator disc plane between the FWVR model and Momentum Theory for load Case I (0),(a),(b).

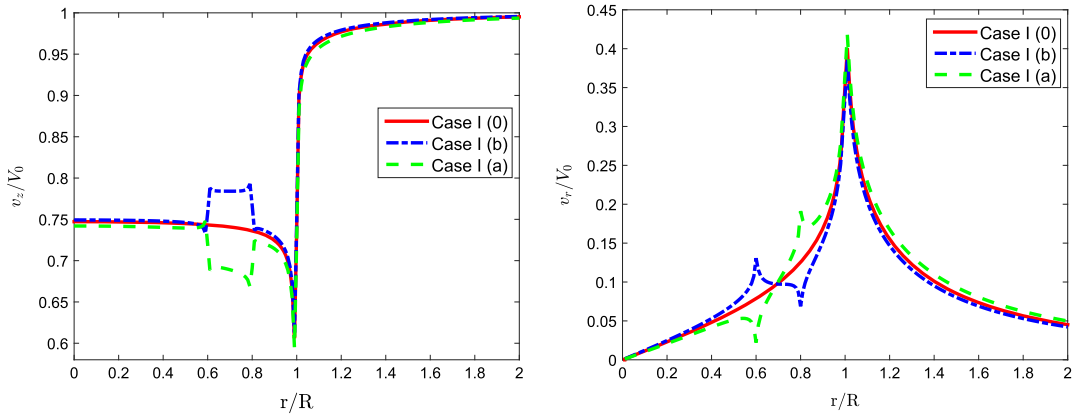

Figure 4. Comparison of the distribution of the axial (left) and the radial (right) velocity at the actuator disc plane from the FWVR model for load Case I (0),(a),(b).

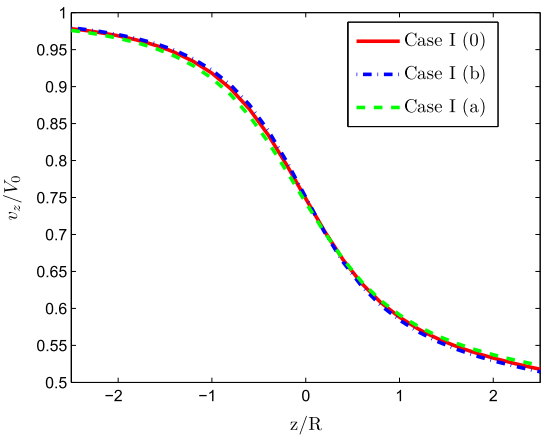

Figure 5. Comparison of the axial velocity along the centreline from the FWVR model for load Case I (0),(a),(b).

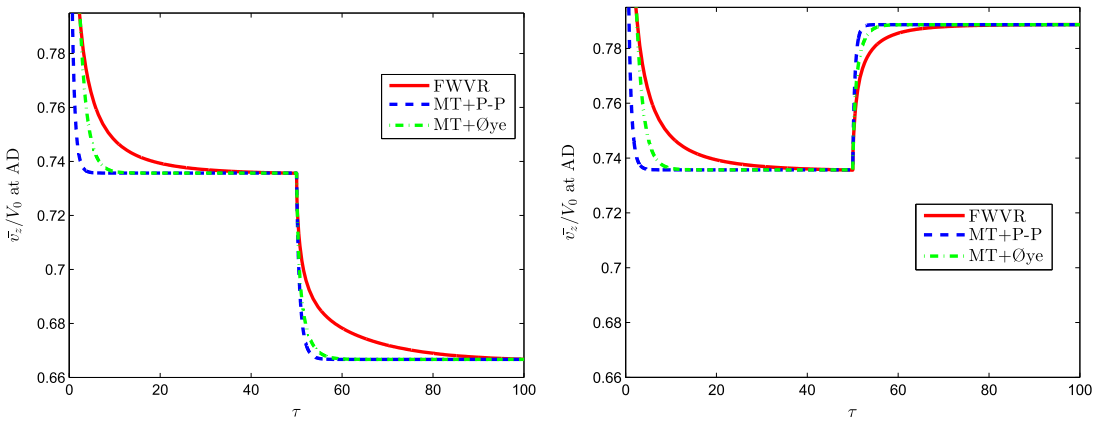

(a) Case II (1)(a) **(b)** Case II (1)(b)

Figure 6. Comparison of averaged axial velocity at the actuator disc between the FWVR model, the Øye and the Pitt-Peters models for Case II (1) (a) and II (1) (b).

in agreement with what was found by Conway[12] that the steady-state value is reached more rapidly for distributions that concentrates load closer to the centre of the actuator disc.

The analysis of the steady radially varied load shows that the main effect of the local load variation is largely confined to the same local region; slight differences outside the local load variation region are present, but they are not significant.

3.2. Analysis for Case II—unsteady uniform load

In this section, the load Case II, two types of unsteady uniform load (1) step time-varying load and (2) harmonically time-varying load are investigated.

3.2.1. Step time-varying load.

Figure 6 shows the averaged axial velocity $\bar{v}_z$ at the actuator disc predicted by the FWVR model, Øye and Pitt-Peters dynamic inflow models for step time-varying uniform load. It is evident that the Pitt-Peters model predicts the smallest time delay, the Øye model predicts a larger time delay than the Pitt-Peters model, and the FWVR model has the largest time delay among all the three for both loading and deloading cases. The difference exists in both the start-up and load transient part, but the start-up part is not the designed load case for the two engineering models. The FWVR predicts larger time delay for the load increased case than that of the load decreased case, which implies that the load strength also has an impact on the time delay.

3.2.2. Harmonically time-varying load.

The results of harmonically time-varying uniform load are analysed here; the simulations are presented for $k = 0.05$, 0.2, 0.5 and 1. Figure 7 compares the hysteresis loops of the averaged axial velocity at the actuator disc from the FWVR model, Momentum Theory, the Pitt-Peters and the Øye dynamic inflow models for Case II (2). The amplitude difference—difference in amplitude of $\bar{v}_z$ from that of the Momentum Theory, and the phase lag—width of the hysteresis loop are mainly analysed.

The dynamic $\bar{v}_z$ is plotted versus thrust coefficient C_t at the actuator disc. Momentum Theory cannot predict any dynamic effect due to its basis of the static state; however, it is plotted here for comparison. As seen for $k = 0.05$, the amplitude of $\bar{v}_z$ predicted by the Pitt-Peters dynamic inflow model matches with the quasi-steady values from the Momentum Theory but has a small phase lag from Momentum Theory. The Øye dynamic inflow model predicts a larger phase lag and amplitude difference than the Pitt-Peters dynamic inflow model, and the FWVR model predicts a even larger phase lag and amplitude difference than the Øye dynamic inflow model. For the larger reduced frequency $k = 0.2$, phase lag and amplitude difference predicted by both engineering models increase, but there is only a visible increase in amplitude difference from the FWVR model. For $k = 0.5$, the amplitude difference increases for all the three models, and the Pitt-Peters model still predicts an increased phase lag, but the phase lag obtained from the Øye model and the FWVR model decreases compared with $k = 0.2$. For $k = 1$, all the three models predict an increased amplitude difference and a decreased phase lag in $\bar{v}_z$ compared with $k = 0.5$.

In general, the frequency of unsteady loads has a significant impact on the dynamic induction. The larger k, the larger amplitude difference compared with Momentum Theory predicted by all the three models. The Øye dynamic inflow model predicts a larger amplitude difference than the Pitt-Peters model, and the FWVR model predicts an even larger amplitude

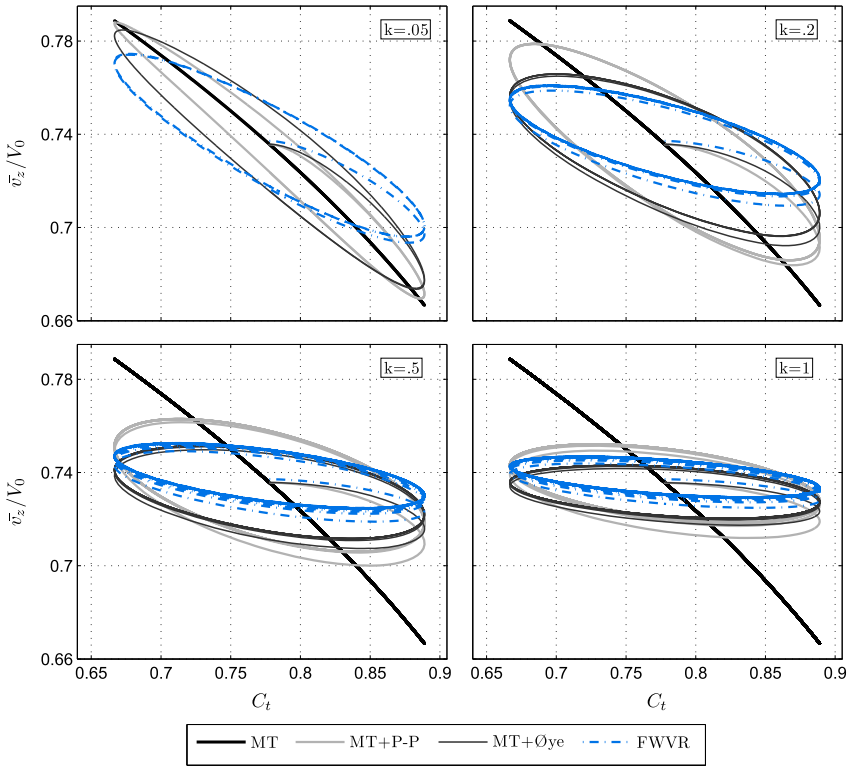

Figure 7. Comparison of hysteresis loops of the averaged axial velocity at the actuator disc between the FWVR model, Momentum Theory, the Øye and the Pitt-Peters models for Case II (2)—an actuator disc undergoing harmonic thrust oscillations with an amplitude of $\Delta C_t = 1/9$ for k = 0.05 ,0.2, 0.5 and 1.

difference than the former. Phase lag predicted by all the three models experiences first an increase and then a decrease as k increases, but the maximum point of k is different for different models. The FWVR model predicts a time delay (both amplitude and phase lag) closer to the Øye model than the Pitt-Peters model. This may be because time constants from the Øye model are also calibrated using a vortex ring model, whereas the Pitt-Peters model is initiated for a helicopter based on a linear model. The difference between the Øye model and FWVR model might be that the constants of Øye model were calibrated for a certain type of rotor with certain loads, they need to be tuned for each case, while the FWVR model is intrinsically applicable for this generic load case.

Figure 8 shows the time series of axial velocity v_z and radial velocity v_r at different annuli obtained from the FWVR model at the reduced frequency of 0.2. As seen, the unsteady load has a similar impact on both axial and radial velocity at different radii, but the extent of the effect is different for different radii; the influence increases from root to tip in both v_z and v_r.

Figure 9 compares the dynamic loop characteristics of v_z between the FWVR model, Momentum Theory and the two engineering dynamic inflow models for different radial positions r/R=0, 0.3, 0.55, 0.6, 0.7, 0.8, 0.85, 0.95 and 0.99, at reduced frequency 0.2. Noticeably, the loop of v_z at different radii from both engineering dynamic inflow models is symmetric to the centre ($C_t = 7/9, v_z = 0.736$), because of the inherent assumption of independent annuli. As the radius is included in equation 17 and 21, they can reflect variations in time delay at different radii. For the Pitt-Peters dynamic inflow model, both the amplitude difference and phase lag increase as the radial position moves from root to tip. The axial velocity from the Pitt-Peters dynamic inflow model coincides with Momentum Theory at the root, because the first term of equation 17 goes to zero at root, which represents the dynamic effect.

Contrary to the Pitt-Peters dynamic inflow model, both amplitude difference and phase lag of the Øye model decrease as the radial position moves outboard, and their range of variation is smaller than that of the Pitt-Peters model. Different from both engineering dynamic inflow models, the centre of v_z at different radii from the FWVR model vary with radial positions because of the non-uniform axial velocity distribution even for the uniform load (Figure 3). The amplitude of v_z predicted by the FWVR model increases as the increase of local radius because of the increasing impact from the tip vorticity. However, there is no discernible variation in phase lag for different positions.

The FWVR model predicts a larger time delay than the two engineering dynamic inflow models for both the step and harmonically time-varying loads of Case II. The difference in the predicted velocity between the FWVR model and

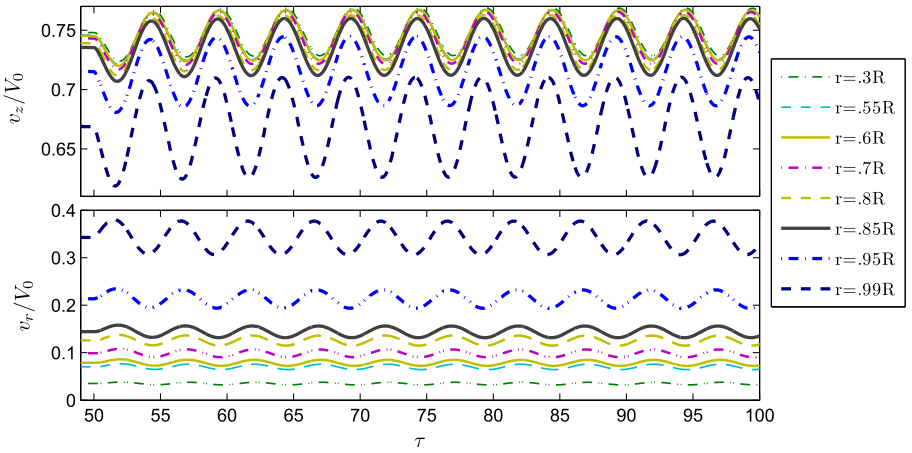

Figure 8. The axial (up) and the radial (down) velocity at different radii from the FWVR model at k =0.2 for Case II (2).

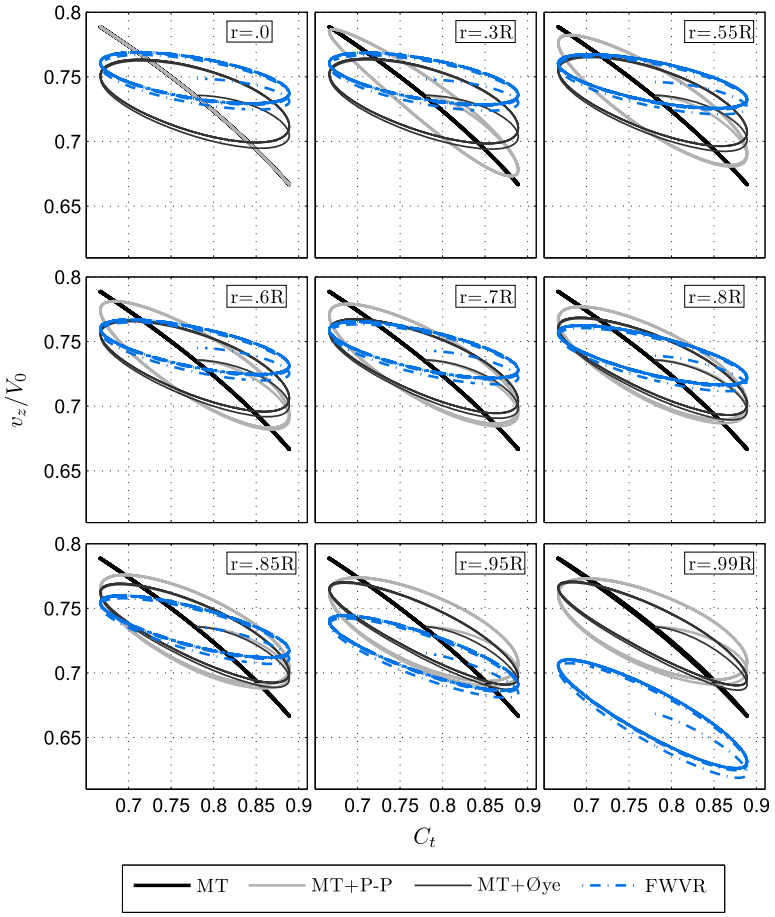

Figure 9. Comparison of hysteresis loops of the axial velocity at different radii between the FWVR model, Momentum Theory and the Øye and Pitt-Peters model for Case II (2) for k = 0.2.

engineering dynamic inflow models indicates that the engineering models needs to be improved or better calibrated for unsteady load effects.

3.3. Analysis for Case III—unsteady radially varied load

In this section, Case III is considered.

Figure 10 compares hysteresis loops of the dynamic axial velocity v_z at 0.7R (the centre of load locally changed region) between the FWVR model, Momentum Theory and the Øye and Pitt-Peters dynamic inflow models. The dynamic velocity v_z is plotted against the thrust coefficient at 0.7R. Loops of v_z at the local annulus predicted by the Øye and the Pitt-Peters dynamic inflow models have a similar pattern as for load Case II (2). The amplitude difference predicted by these models increases as the increase of k. The phase lag first increases and then decreases as k increases. However, the phase lag is very small in the local velocity v_z from the FWVR model for all reduced frequencies, and the amplitude difference from the FWVR model also changes slightly with k. The difference in v_z between the FWVR model and Momentum Theory increases as the increase of thrust coefficient. This implies again that the time delay relates to the thrust strength.

The biggest difference for Case III from Case II (2) is that the FWVR model predicts much smaller phase lag in this unsteady radially varied load case. This is because the shed vortices at 0.6R and 0.8R are with the same strength but opposite signs (as indicated in Figure 1), the difference in phase lag induced by them partially cancels out. The main reason behind the difference between the FWVR model and the two engineering dynamic inflow models for this case is that both engineering dynamic inflow models have been developed for an actuator disc with uniform load, but they are extended to radial annuli assuming annuli independent as in BEM, while the FWVR model can inherently account for load radially varied effects. Therefore, the dynamic inflow models, which are extended to an actuator annulus based on the independent annuli assumption, should be improved for localized unsteady loads.

Figure 11 shows v_z and v_r at different radii for $k = 0.2$. The effect on v_z at the region with the time-varying load, $0.6R - 0.8R$, is prominent, especially the centre of this area, 0.7R. Another phenomenon is that the locally varied unsteady load has more effect on v_z at the outboard part than that at the inboard part, even when they are at the same distance from

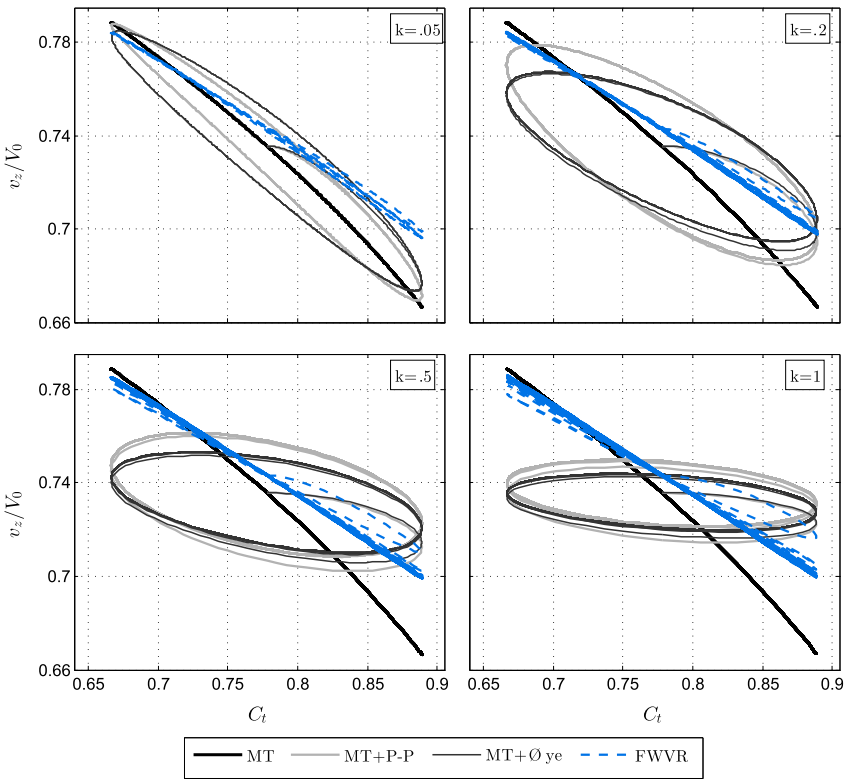

Figure 10. Comparison of hysteresis loops of the axial velocity at 0.7R between the FWVR model, Momentum Theory and the Øye and the Pitt-Peters models for Case III—an actuator disc undergoing harmonic thrust oscillations in the annulus region $0.6R - 0.8R$ with an amplitude of $\Delta C_t = 1/9$ for k = 0.05, 0.2, 0.5 and 1.

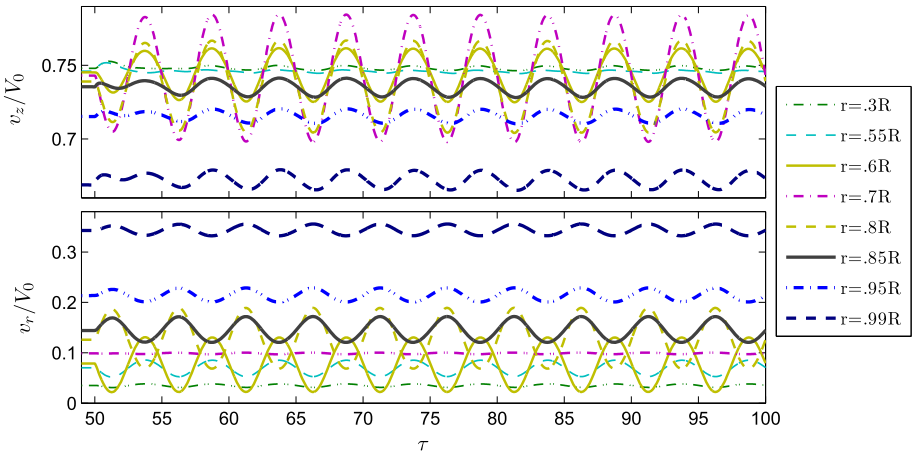

Figure 11. The axial (up) and the radial (down) velocity from the FWVR model at different radii at k =0.2 for Case III.

the load changing area, for example, 0.55R and 0.85R. The trend of v_r is different from that of v_z. The centre, 0.7R, is least affected as shed vortices at 0.6R and 0.8R are anti-phase but with the same strength, the radial induced velocity by them at 0.7R are partially cancelled out. That v_r at different sides from the centre 0.7R changes with opposed phase can be explained by the same reason, vortex shed at 0.6R dominates the inboard part, vortex shed at 0.8R dominates the outboard part. The average v_r increases with the increasing local radius, which is consistent with Figure 4 (b).

Figure 12 compares the dynamic loop characteristics of v_z given by the FWVR model, Momentum Theory and the two engineering dynamic inflow models for different radii for the reduced frequency of 0.2. The locally varied load has an influence on v_z at any radial position calculated by the FWVR model, which has been already known from Figure 11. However, the dynamic effects on v_z predicted by the two engineering dynamic inflow models is in the region restricted to the local area $0.6R - 0.8R$; outside this region, the velocity predicted by them coincides exactly with Momentum Theory. The difference of v_z at radii outside the load varying area between the FWVR model and Momentum Theory and the two engineering models confirms again that the independent annuli assumption has an impact. Comparing Figure 9 with Figure 12, it is known that the local unsteady load has a significantly different influence on the dynamic velocity at every annulus compared with the uniform dynamic load. This further emphasizes that the use of independent annuli assumption-based dynamic inflow models are insufficient for the induction calculation of localized unsteady load.

3.4. Aerodynamic work

The impact of the different dynamic induction from different models on the aerodynamic work is discussed in this section. The results are much different from that of Madsen and Rasmussen.[10] In addition to the difference caused by different free wake models, the main reason is that the work is calculated in a different way in this paper. Madsen and Rasmussen[10] assumed that the harmonic thrust on the blade is caused by a harmonic translation of the rotating blade with an amplitude of 1 m, and the work is calculated by integrating this load at this translation distance. However, this paper starts from the energy harvesting point of view; there is no assumption between load and disc motion. Under the distributed force on the actuator disc prescribed in Table I, the rate of work carried out by the force is $\int f v_z dA$. Therefore, the work (W) carried out on the disc by the air in one harmonic cycle is given by

$$W = \int_{\Delta T} \int_{A} (f \cdot v_z) dA dt. \tag{22}$$

When normalized to the work can be performed on the disc without any induction, a new term, the coefficient of relative work (C_{rw}), is defined here

$$C_{rw} = \frac{W}{\int_{\Delta T} \int_{A} (f \cdot V_0) dA dt}. \tag{23}$$

The definition of the denominator has no practical meaning, it is used for nondimensionalization here. Both load Case II (2) and Case III are investigated here. Where A is the area of the disc for Case II (2), but the area of the local annulus of $0.6R - 0.8R$ for Case III. The third cycle is chosen for integration to obtain a stable induction. The results are plotted in Figure 13.

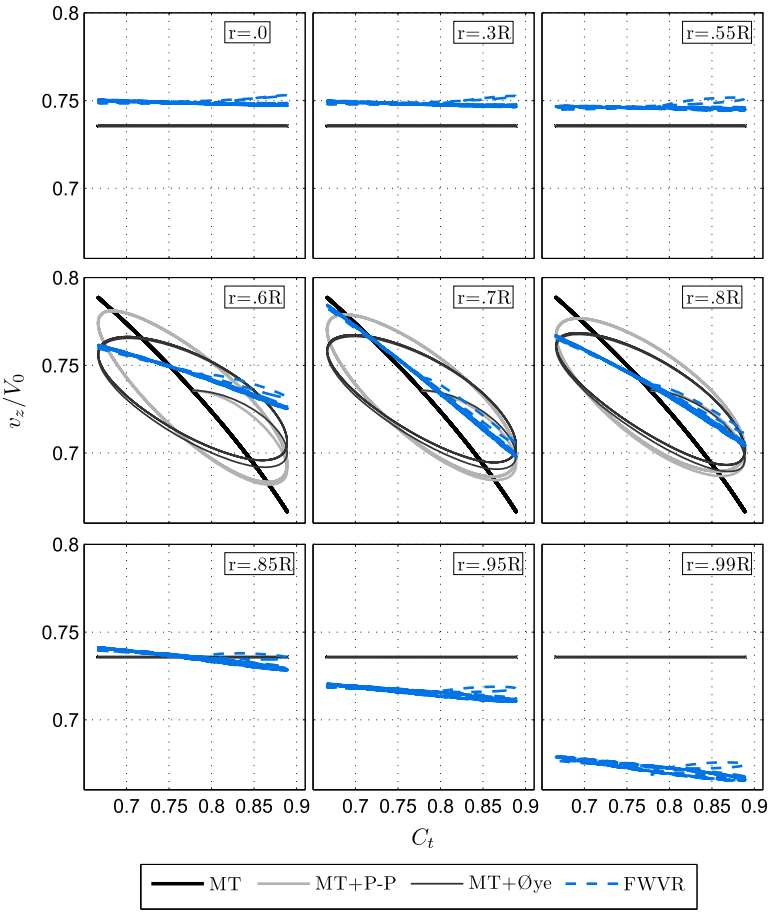

Figure 12. Comparison of hysteresis loops of the axial velocity at different radii between the FWVR model, Momentum Theory, and the Øye and the Pitt-Peters models for Case III for k = 0.2.

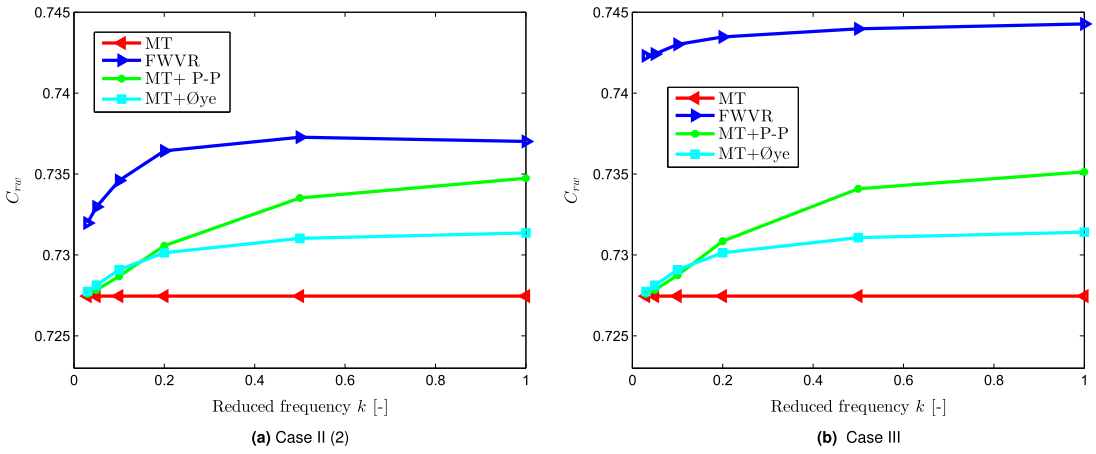

Figure 13. Comparison of relative work of the aerodynamic thrust force from Momentum Theory, the FWVR model and the Øye and the Pitt-Peters models.

As seen, the two engineering models predict no difference in two different load cases because they are based on the assumption of annuli independence. The Øye model predicts higher aerodynamic work than Momentum Theory, and the Pitt-Peters model predicts even higher aerodynamic work than the Øye model at high frequencies for both cases, which

is consistent with the area formed by the loops and the coordinates in Figures 7 and 10. C_{rw} from Momentum Theory is at a constant value of 0.7275 for both Case II (2) and Case III for all frequencies, which is 0.2725 lower than that when induction is not considered. This is consistent with the velocity deficit at the actuator disc induced by the cylindrical wake of Momentum Theory ($a = 0.2643$ for $C_t = 7/9$); the difference of 0.0082 is caused by the non-linear relationship between C_t and a in Momentum Theory.

For Case II (2), the FWVR model predicts higher aerodynamic work than Momentum Theory and the two engineering models. Moreover, for Case III, the FWVR model predicts even higher aerodynamic work. Momentum Theory is based on the steady assumption; it predicts constant aerodynamic work for all frequencies. As expected, when the frequency decreases, the flow field approaches a quasi-steady state, aerodynamic work from the two engineering models, and the FWVR model approaches that of Momentum Theory in both load Cases. However, the relative work from the FWVR model for the smallest considered frequency $k = 0.03$ even does not coincide with that from Momentum Theory, which means the FWVR model predicts a different threshold value to consider the flow quasi-steady than the engineering models.

The two engineering models, which are extended from an actuator disc to annular-level (based on the annuli independence assumption), predict exactly the same relative aerodynamic work in both Case II (2) and Case III. The higher relative aerodynamic work from the FWVR model in both Case II (2) and Case III shows that the engineering dynamic inflow models underestimate the energy that can be extracted from the air, especially for radially varied load case.

4. CONCLUSION AND FUTURE WORK

A free wake model has been developed for the calculation of the induced velocity field of an actuator disc with radially varied and unsteady loads. The model is composed of free wake vortex rings for the near wake and semi-infinite cylindrical vortex tubes for the far wake. This FWVR model has been applied to three load cases: (i) steady uniform and radially varied load, (ii) two types of unsteady uniform load and (iii) unsteady radially varied load.

Comparison of results between the FWVR model, Momentum Theory and two engineering dynamic inflow models of the Pitt-Peters and Øye leads to the following main conclusions.

For Case I, the velocity field is predictably most affected at the areas where there is load variation, with an insignificant effect on other radial positions. For Case II, the FWVR model predicts a larger time delay than the two engineering dynamic inflow models for both step and harmonically time-varying loads.

For Case III, the velocity obtained from both engineering dynamic inflow models follow a same trend, leading to the same trend in aerodynamic work as for Case II (2). However, the FWVR model predicts significant differences of v_z from Momentum Theory and the two engineering dynamic inflow models for Case III, which results even higher relative aerodynamic work. This means that the engineering dynamic inflow models underestimate the energy that can be extracted from the air, especially for localized unsteady load.

The small difference in predicted velocity between Momentum Theory and the FWVR model proves that Momentum Theory and the independent annuli assumption is acceptable for steady load. The larger time delay from the FWVR model for the unsteady uniform load and the resulting different aerodynamic work between the FWVR model and the two engineering dynamic inflow models in the harmonically time-varying load indicates that these engineering models should be improved or better tuned for unsteady load analysis. The significant difference in the dynamic velocity and aerodynamic work between the FWVR model and the two engineering models for the unsteady radially varied load reveals that both engineering dynamic inflow models, which are based on the assumption of independent annuli, are not sufficient for investigation of localized unsteady loads. Improving the existing engineering models or developing more advanced models are needed.

This paper has considered an actuator disc case. For future work, the relationship between load strength and time delay, the effect of rotation, finite number of blades, the interaction of tip vortex and vortex shedding from trailing edge flaps will be explored. Azimuthwise varied loading due to shear, yaw or turbulent flow is also of interest. The conclusions of this paper are based on the validity of the vortex ring model against steady actuator disc measurements; however, its efficacy in unsteady loading is still pending. Experiments of actuator disc model undergoing unsteady loading are designed to further verify this.

APPENDIX A

This appendix addresses the two convergence issues of the FWVR model. The first one is the effect of parameters used in the model, mainly the time step and cut-off. The second one is the effect of the extension of the shed vortex rings.

Results show $\bar{v}_z$ at the actuator disc to decrease monotonously with time. At time $\tau = 50$, the difference from Momentum Theory in $\bar{v}_z$ at actuator disc for $C_t = 7/9$ is less than 0.5%, and the decreasing rate $\frac{d(\bar{v}_z(50))}{d\tau}$ is at 9e-6. Therefore, $\bar{v}_z(50)$ at actuator disc for $C_t = 7/9$ for these verification cases are checked. Figure A1 shows $\bar{v}_z(50)$ at the actuator disc using five different cut-off radii $\delta = 1e-3, 1e-4, 1e-5, 1e-6, 1e-7$ and six different time steps

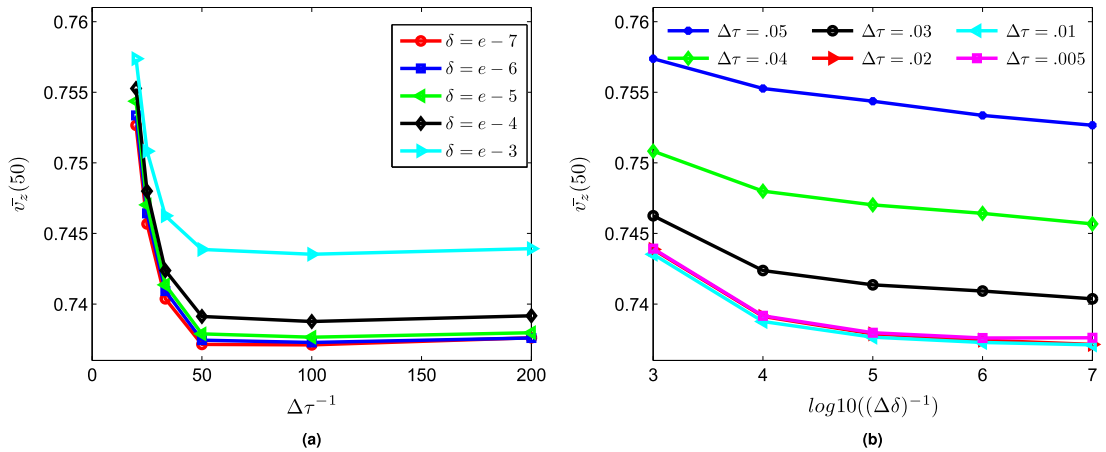

Figure A1. Convergence of the averaged velocity at the actuator disc at $\tau = 50$ inverse (a) time step, inverse (b) cut-off radius, for $C_t = 7/9$ (The curve for $\Delta\tau = 0.02$ almost coincides with that for $\Delta\tau = 0.01$).

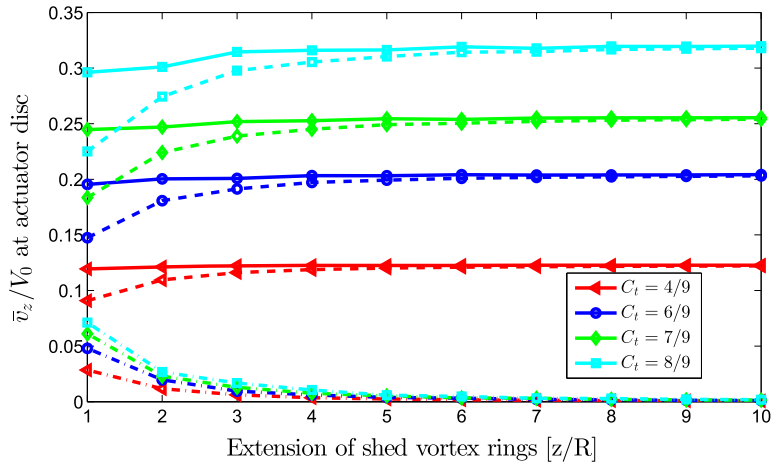

Figure A2. Averaged induced velocity at the actuator disc from the vortex rings (dash line), the semi-infinite vortex tube (dash dot line) and the total (solid line) for different extensions of vortex rings, for $C_t = 4/9, 6/9, 7/9, 8/9$.

$\Delta\tau = 0.05, 0.04, 0.03, 0.02, 0.01, 0.005$. When the cut-off is smaller than $\delta = 1e-5$, the difference of $\bar{v}_z(50)$ from that of Momentum Theory is within 0.2%. The difference in $\bar{v}_z(50)$ is less than 0.1% for time steps smaller than $\Delta\tau = 0.02$, which give confidence in using $\Delta\tau \leq 0.02$ and $\delta \leq 1e-5$ for all the simulations.

The influence of the extension of the shed vortex rings on the convergence of the averaged axial induced velocity $\bar{v}_z$ at the disc is shown in Figure A2. It shows the contribution from the semi-infinite vortex tube, from the vortex rings and from the total to $\bar{v}_z$ at the actuator disc for different extensions of the shed vortex rings, for $C_t = 4/9, 6/9, 7/9, 8/9$. A larger extension of the vortex rings increases its contribution to the total induction, as the contribution from the semi-infinite vortex tube become less significant. However, the total induction from both vortex rings and the semi-infinite vortex tube converges after certain extensions of vortex rings. Although a longer extension is needed for a larger thrust to converge, the total induction $\bar{v}_z$ converges at 10R for all considered thrust coefficients. Therefore, it is reasonable to replace the far wake with a semi-infinite vortex tube after 10R.

Figure A3 shows the location of the vortex rings of the fully developed near wake for $C_t = 4/9, 6/9, 7/9, 8/9$, where instability can be seen downstream. The larger the thrust, the longer the distance is for a complete wake expansion. The dot line shows the ideal radius in the infinite far wake from Momentum Theory. Taking into account, the convergence of the total $\bar{v}_z$ in Figure A2 and the locations of the core of the vortices, the semi-infinite vortex tube starts from around 11R (shown in Figure A3) for all these thrust coefficients. At these places, the FWVR model has a converged $\bar{v}_z$, and the ideal wake radius can be used as radius of the semi-infinite vortex tube.

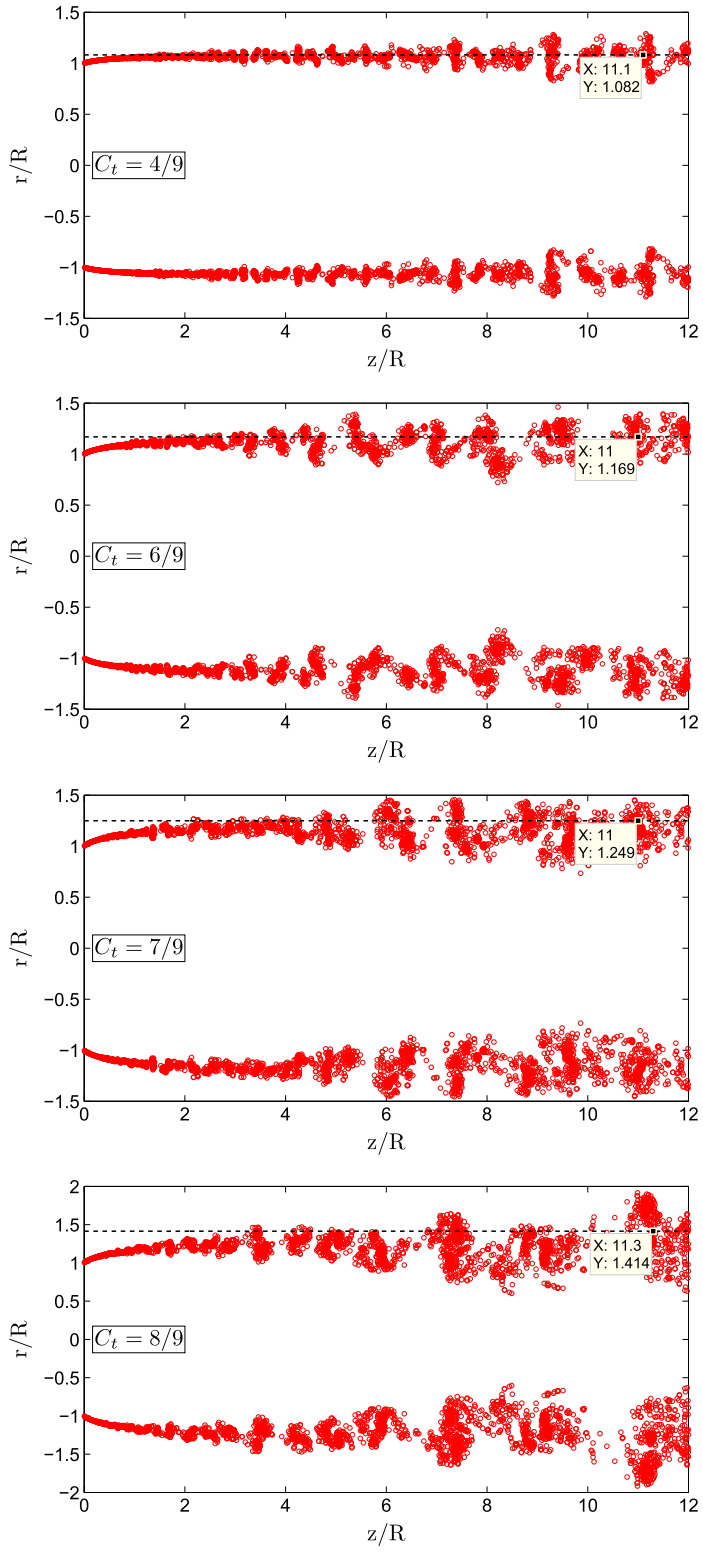

Figure A3. Location of vortex rings in the fully developed near wake for C_t=4/9, 6/9, 7/9, 8/9. Points represent intersections of the rings with the symmetry plane. Dotted lines show the ideal radius in infinite far wake from Momentum Theory.

APPENDIX B

The validity of the FWVR model is addressed in this appendix. Velocity field of an actuator disc represented by a porous mesh was measured by Lignarolo *et al.*[25] The experiments were conducted in the Φ 3 m Open Jet Facility (OJF) at the Delft University of Technology. The wind speed was 4.7 m/s, the corresponding Reynolds number to the disc diameter of 0.6 m is 188000. The porosity of the disc made by three layers of metal mesh is 60%; the thrust measured by a force balance is $C_t = 0.93$. The three-component velocity field of the disc were obtained with a stereoscopic particle image velocimetry (SPIV). The experiment was also used to benchmark four large eddy simulation (LES) codes and a vortex model for the flow field of the near wake of an actuator disc.[26] The measured time-averaged axial velocity field is shown in Figure B1, the intersections of the vortex rings with the symmetry plane are represented by black points. The blank region immediately aft the disc was not covered by the measurements. The expansion from the FWVR model matches with the tunnel measurement well. Notably, the $C_t = 0.93$ is high, which leads to earlier start of the instability from the FWVR model. The vortex rings start to roll up at around $x/R = 1.0$, while still remaining within the shear layer of the measured wake of the actuator disc model.

Figure B2 compares the velocity at planes of z/R=-0.5,0.2,1.5,3.0,4.5 between the FWVR model and the measurements for $C_t = 0.93$. The FWVR model captures the velocity profile generally well. Because of the lack of turbulence dissipation

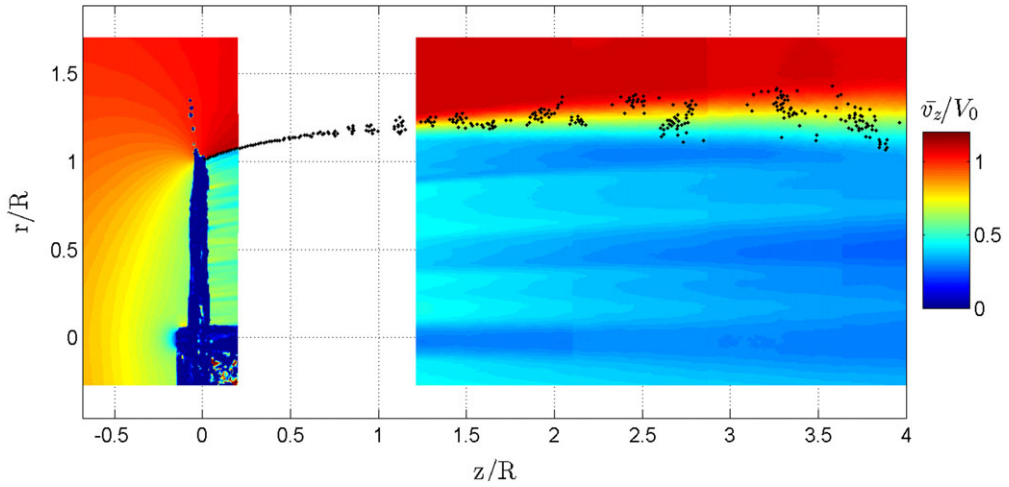

Figure B1. Comparison between positions of vortex rings from the FWVR model and time averaged velocity field from the wind tunnel measurements of an actuator disc for $C_t = 0.93$. Black points represent intersections of the vortex rings with the symmetry plane

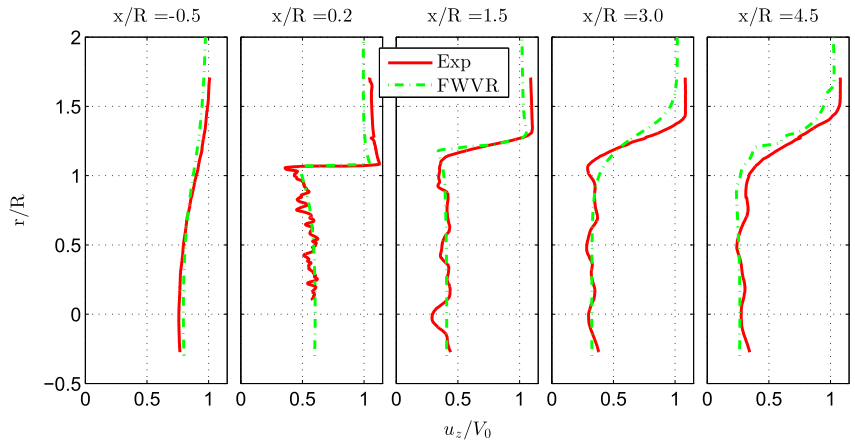

Figure B2. Velocity comparison between the FWVR model and wind tunnel measurements at planes of $x/R = -0.5, 0.2, 1.5, 3.0, 4.5$ for $C_t = 0.93$

in the FWVR model, the experimental velocity distribution at the edge of the wake is smoother. As the same as the four large eddy simulation codes and the vortex model in Lignarolo *et al.*,[26] the velocity values outside the wake from the FWVR model are lower than experimental results.

ACKNOWLEDGEMENT

The first author gratefully acknowledges financial support from China Scholarship Council.

REFERENCES

1. Hansen M, Sørensen J, Voutsinas S, Sørensen N, Madsen H. State of the art in wind turbine aerodynamics and aeroelasticity. *Progress in Aerospace Sciences* 2006; **42**(4): 285–330.
2. Snel H, Schepers J. Engineering models for dynamic inflow phenomena. *Journal of Wind Engineering and Industrial Aerodynamics* 1992; **39**(1-3): 267–281.
3. Schepers J, Snel H, *Dynamic inflow: yawed conditions and partial span pitch control*, Technical Report, 1995.
4. Snel H, Schepers J, *Joint investigation of dynamic inflow effects and implemention of an engineering method*, Technical Report, 1995.
5. Sørensen J, Myken A. Unsteady actuator disc model for horizontal axis wind turbines. *Journal of Wind Engineering and Industrial Aerodynamics* 1992; **39**(1-3): 139–149.
6. Chattot JJ. Actuator disk theory steady and unsteady models. *Journal of Solar Energy Engineering* 2014; **136**(3): 1–10.
7. Sørensen J, Kock C. A model for unsteady rotor aerodynamics. *Journal of Wind Engineering and Industrial Aerodynamics* 1995; **58**: 259–275.
8. Sørensen J, Mikkelsen R. On the validity of the blade element momentum method. *European Wind Energy Conference*, Copenhagen, 2001; 362–366.
9. Madsen H. A CFD analysis of the actuator disc flow compared with BEM. *Proceedings of the 10th Symposium on Aerodynamics of Wind Turbines*, 1996; 109–124.
10. Madsen H, Rasmussen F. A near wake model for trailing vorticity compared with the blade element momentum theory. *Wind Energy* 2004; **7**(4): 325–341.
11. van Kuik G, Lignarolo L. Potential flow solutions for energy extracting actuator disc flows. *Wind Energy* 2015. doi: 10.1002/we.1902.
12. Conway J. Analytical solutions for the actuator disk with variable radial distribution of load. *Journal of Fluid Mechanics* 1995; **297**: 327–355.
13. Conway J. Exact actuator disk solutions for non-uniform heavy loading and slipstream contraction. *Journal of Fluid Mechanics* 1998; **365**: 235–267.
14. Froude R. On the part played in propulsion by differences of fluid pressure. *Institution of Naval Architects* 1889; **30**: 390–405.
15. van Kuik G. The edge singularity of an actuator disc with a constant normal load. *22nd AIAA/ASME Wind Energy Symposium*, Reno, USA, 2003–0356.
16. Øye S. A simple vortex model of a turbine rotor. *Proceedings of the 3rd IEA Symposium on the Aero-Dynamics of Wind Turbines*, Harwell, 1990; 1–15.
17. Yoon S, Heister S. Analytical formulas for the velocity field induced by an infinitely thin vortex ring. *International Journal for Numerical Methods in Fluids* 2004; **44**: 665–672.
18. Abramowitz M, Stegun I, *Handbook of mathematical functions*, 1972.
19. Leishman J, Bhagwat MJ, Baga A. Free-vortex filament methods for the analysis of helicopter rotor wakes. *Journal of Aircraft* 2002; **39**(5): 759–775.
20. Baldacchino D. Horizontal Axis Wind Turbine (HAWT) wake stability investigations, *Msc thesis*, Delft University of Technology, 2012.
21. Paxton F. Solid angle calculation for a circular disk. *The Review of Scientific Instruments* 1959; **30**(4): 254–258.
22. Branlard E, Gaunaa M. Cylindrical vortex wake model : right cylinder. *Wind Energy* 2015; **18**(11): 1973–1987.
23. Pitt D, Peters D. Theoretical prediction of dynamic-inflow derivatives. *Vertica* 1981; **5**(1): 21–34.
24. Leishman J. Challenges in modelling the unsteady aerodynamics of wind turbines. *Wind Energy* 2002; **5**(2-3): 85–132.
25. Lignarolo L, Ragni D, Ferreira C, van Bussel G. Experimental comparison of a wind turbine and of an actuator disc wake. *Journal of Renewable and Sustainable Energy* 2016; **8**: 1–27.

26. Lignarolo L, Mehta D, Stevens R, Yilmaz A, Van Kuik GAM, Andersen SJ, Meneveau C, Ferreira C, Ragni D, Meyers J, *et al.* Validation of four LES and a vortex model against stereo-PIV measurements in the near wake of an actuator disc and a wind turbine. *Renewable Energy* 2016; **94**: 510–523.